Citation: Matoza, R.S., D. Fee, J.D. Assink, A.M. Iezzi, D.N. Green, K. Kim, L. Toney, T. Lecocq, S. Krishnamoorthy, J.-M. Lalande, K. Nishida, K.L. Gee, M.M. Haney, H.D. Ortiz, Q. Brissaud, L. Martire, L. Rolland, P. Vergados, A. Nippress, J. Park, S. Shani-Kadmiel, A. Witsil, S. Arrowsmith, C. Caudron, S. Watada, A.B. Perttu, B. Taisne, P. Mialle, A. Le Pichon, J. Vergoz, P. Hupe, P.S. Blom, R. Waxler, S. De Angelis, J.B. Snively, A.T. Ringler, R.E. Anthony, A.D. Jolly, G. Kilgour, G. Averbuch, M. Ripepe, M. Ichihara, A. Arciniega-Ceballos, E. Astafyeva, L. Ceranna, S. Cevuard, I.-Y. Che, R. De Negri, C.W. Ebeling, L.G. Evers, L.E. Franco-Marin, T.B. Gabrielson, K. Hafner, R.G. Harrison, A. Komjathy, G. Lacanna, J. Lyons, K.A. Macpherson, E. Marchetti, K.F. McKee, R.J. Mellors, G. Mendo-Pérez, T.D. Mikesell, E. Munaibari, M. Oyola-Merced, I. Park, C. Pilger, C. Ramos, M.C. Ruiz, R. Sabatini, H.F. Schwaiger, D. Tailpied, C. Talmadge, J. Vidot, J. Webster, D.C. Wilson (2022), Atmospheric waves and global seismoacoustic observations of the January 2022 Hunga eruption, Tonga, Science, doi:10.1126/science.abo7063

Title: Atmospheric waves and global seismoacoustic observations of the January 2022 Hunga eruption, Tonga

Authors:

Robin S. Matoza[1*], David Fee[2], Jelle D. Assink[3], Alexandra M. Iezzi[1], David N. Green[4], Keehoon Kim[5], Liam Toney[2], Thomas Lecocq[6], Siddharth Krishnamoorthy[7], Jean-Marie Lalande[8], Kiwamu Nishida[9], Kent L. Gee[10], Matthew M. Haney[11], Hugo D. Ortiz[1], Quentin Brissaud[12], Léo Martire[7], Lucie Rolland[13], Panagiotis Vergados[7], Alexandra Nippress[4], Junghyun Park[14], Shahar Shani-Kadmiel[3], Alex Witsil[2], Stephen Arrowsmith[14], Corentin Caudron[15], Shingo Watada[9], Anna B. Perttu[16,17], Benoit Taisne[16,18], Pierrick Mialle[19], Alexis Le Pichon[20], Julien Vergoz[20], Patrick Hupe[21], Philip S. Blom[22], Roger Waxler[23], Silvio De Angelis[24], Jonathan B. Snively[25], Adam T. Ringler[26], Robert E. Anthony[26], Arthur D. Jolly[27], Geoff Kilgour[28], Gil Averbuch[14], Maurizio Ripepe[29], Mie Ichihara[9], Alejandra Arciniega-Ceballos[30], Elvira Astafyeva[31], Lars Ceranna[21], Sandrine Cevuard[32], Il-Young Che[33], Rodrigo De Negri[1], Carl W. Ebeling[34], Läslo G. Evers[3], Luis E. Franco-Marin[35], Thomas B. Gabrielson[36], Katrin Hafner[37], R. Giles Harrison[38], Attila Komjathy[7], Giorgio Lacanna[29], John Lyons[11], Kenneth A. Macpherson[2], Emanuele Marchetti[29], Kathleen F. McKee[39], Robert J. Mellors[34], Gerardo Mendo-Pérez[40], T. Dylan Mikesell[41], Edhah Munaibari[13], Mayra Oyola-Merced[7], Iseul Park[33], Christoph Pilger[21], Cristina Ramos[42], Mario C. Ruiz[42], Roberto Sabatini[25], Hans F. Schwaiger[11], Dorianne Tailpied[16], Carrick Talmadge[23], Jérôme Vidot[8], Jeremy Webster[22], David C. Wilson[26]

*Corresponding author. Email: rmatoza@ucsb.edu

Affiliations:

1. Department of Earth Science and Earth Research Institute, University of California, Santa Barbara, CA, USA
2. Wilson Alaska Technical Center and Alaska Volcano Observatory, Geophysical Institute, University of Alaska Fairbanks, Fairbanks, AK, USA
3. R&D Department of Seismology and Acoustics, Royal Netherlands Meteorological Institute (KNMI), De Bilt, the Netherlands
4. AWE Blacknest, Brimpton, Reading, RG7 4RS, UK
5. Lawrence Livermore National Laboratory, Livermore, CA, USA
6. Seismology - Gravimetry, Royal Observatory of Belgium, Belgium
7. NASA Jet Propulsion Laboratory, California Institute of Technology, 4800 Oak Grove Dr, Pasadena, CA 91109, USA
8. CNRM, Université de Toulouse, Météo-France, CNRS, Lannion, France
9. Earthquake Research Institute, University of Tokyo, Tokyo, Japan
10. Department of Physics and Astronomy, Brigham Young University, Provo, Utah, USA
11. U.S. Geological Survey, Alaska Volcano Observatory, Anchorage, AK, USA, 99508
12. NORSAR, Kjeller, Norway

13. Université Côte d'Azur, Observatoire de la Côte d'Azur, CNRS, IRD, Géoazur, 250 rue Albert Einstein, Sophia Antipolis 06560 Valbonne, France.

14. Roy M. Huffington Department of Earth Sciences, Southern Methodist University, Dallas, Texas, U.S.A

15. Laboratoire G-Time, Department of Geosciences, Environment and Society, Université libre de Bruxelles, Belgium

16. Earth Observatory of Singapore, Nanyang Technological University, Singapore

17. Volcanic Risk Solutions, Massey University, Palmerston North, New Zealand

18. Asian School of the Environment, Nanyang Technological University, Singapore

19. Comprehensive Nuclear-Test-Ban Treaty Organisation, Vienna, Austria

20. CEA, DAM, DIF, F-91297 Arpajon, France

21. BGR (Federal Institute for Geosciences and Natural Resources), Hannover, Germany

22. Geophysics Group, Los Alamos National Laboratory, Los Alamos, NM, USA

23. National Center for Physical Acoustics, University of Mississippi, University, MS, USA

24. School of Environmental Sciences, University of Liverpool, Liverpool, UK

25. Department of Physical Sciences and Center for Space and Atmospheric Research (CSAR), Embry-Riddle Aeronautical University, Daytona Beach, Florida, USA

26. USGS Albuquerque Seismological Laboratory, Albuquerque, NM, USA

27. USGS Hawaiian Volcano Observatory, Suite A8, 1266 Kamehameha Avenue, Hilo, HI, USA

28. GNS Science, Wairakei Research Centre, Taupō, New Zealand

29. Department of Earth Sciences, University of Florence, Florence, Italy

30. Departamento de Vulcanología, Instituto de Geofísica, Universidad Nacional Autónoma de México, México.

31. Université de Paris, Institut de Physique du Globe de Paris, 35-39 Rue Hélène Brion, 75013 Paris, France

32. Vanuatu Meteorology and Geohazards Department, Port Vila, Vanuatu

33. KIGAM (Korea Institute of Geoscience and Mineral Resources), Daejeon, Korea

34. Institute of Geophysics and Planetary Physics, Scripps Institution of Oceanography, University of California, San Diego, La Jolla, California, USA

35. Volcanological Observatory of the Southern Andes, National Geology and Mining Service (OVDAS, Sernageomin), Chile

36. Graduate Program in Acoustics, Penn State University, State College, PA, USA

37. Incorporated Research Institutions for Seismology (IRIS), Washington, DC, USA

38. Department of Meteorology, University of Reading, UK

39. NASA Goddard Space Flight Center, Greenbelt, MD, USA

40. Posgrado en Ciencias de la Tierra, Universidad Nacional Autónoma de México, Mexico City, Mexico

41. Norwegian Geotechnical Institute (NGI), Oslo, Norway

42. Instituto Geofísico, Escuela Politécnica Nacional, Ecuador

Abstract: The 15 January 2022 climactic eruption of Hunga volcano, Tonga produced an explosion in the atmosphere of a size that has not been documented in the modern geophysical record. The event generated a broad range of atmospheric waves observed globally by various ground-based and spaceborne instrumentation networks. Most prominent is the surface-guided Lamb wave (≲0.01 Hz), which we observed propagating for four (+three antipodal) passages around the Earth over six days. Based on Lamb wave amplitudes, the climactic Hunga explosion was comparable in size to that of the 1883 Krakatau eruption. The Hunga eruption produced remarkable globally-detected infrasound (0.01–20 Hz), long-range (~10,000 km) audible sound, and ionospheric perturbations. Seismometers worldwide recorded pure seismic and air-to-ground coupled waves. Air-to-sea coupling likely contributed to fast-arriving tsunamis. We highlight exceptional observations of the atmospheric waves.

One-Sentence Summary: Global multi-technology observations of atmospheric and seismic waves from the explosive eruption of Hunga

Main Text:

The 15 January 2022 eruption of Hunga volcano (*1*), Tonga was an unusually energetic explosive event. This climactic eruption (the largest eruption of an episode) began just after ~04:00 UTC (~17:00 local time) from a submerged vent and delivered volcanic tephra and gas primarily into the stratosphere. An umbrella cloud developed at approximately 30 km above sea level, with a central transient overshoot much higher. Hunga is a largely submerged massif located ~65 km to the north-northwest of Tongatapu, Kingdom of Tonga. Eruption episodes consisting of relatively low-energy Surtseyan activity in 2009 and 2014–2015 had built a tephra cone that connected the established islands of Hunga Tonga and Hunga Ha'apai on the northwestern portion of the massif (*2*). Surtseyan eruptions transitioned into violent, impulsive eruptions from 19 December 2021 as part of the most recent episode. The climactic 15 January eruption produced a broad range of atmospheric waves observed globally by numerous ground-based and spaceborne instrumentation systems, including atmospheric pressure sensors, seismometers, hydrophones, Global Navigation Satellite System (GNSS) receivers, and weather satellites (Fig. 1A) (*3*). We highlight exceptional multi-technology observations of this extraordinary event in the modern digital record and provide initial interpretations of the atmospheric wave types generated and their propagation around the globe.

The onset of the most recent eruptive episode is characterized remotely by seismicity and co-eruptive infrasound on 19 December 2021, preceded by seismic activity on 18 December 2021 (16:49:46 UTC, body-wave magnitude *mb* 4.0) (Fig. 1B) (*3*). Eruptive activity continued until 4 January 2022, with decreasing infrasonic amplitudes at International Monitoring System (IMS) infrasound station IS22 (1,848 km) and intermittent detections by IMS hydroacoustic stations. Powerful eruptive infrasound activity resumed on 13 January 2022, with amplitudes ~10 times that of the December activity. Infrasound continued on 14 January accompanied by seismic tremor (*3*) (fig. S2A,B); infrasound amplitudes subsequently decreased while the number of hydroacoustic *T*-phase detections increased. Following brief relative quiescence, at least four IMS hydroacoustic (fig. S3), all 53 IMS infrasound, and numerous seismic stations detected the main climactic eruption on 15 January 2022 (04:14:45 UTC, moment-magnitude M_w 5.7–5.8, Table S1). Regional infrasound, barometer, and volcanic plume observations suggest a complex eruption sequence occurring between 04:00 and ~04:30, not just a single onset or explosion (Figs. 1A,2E,3A). A last major eruption at ~08:31 UTC 15 January was detected by at least 20 IMS infrasound and two IMS hydroacoustic stations, after which the volcanic activity decreased.

Atmospheric waves (*4*) are propagating mechanical perturbations in the atmospheric fluid. Nonlinearities in the propagation cause the spectrum to evolve (i.e., energy cascading), and may result in shock-wave formation and period lengthening. Gravity waves are disturbances to the balance between buoyancy and gravity (frequency $f \lesssim 3$ mHz); acoustic waves manifest as propagating compressions and rarefactions ($f \gtrsim 4$ mHz). These different physical mechanisms lead to different propagation speeds. Acoustic-gravity waves (AGWs) are waves exhibiting both buoyant and compressional motion (*5*), typically with mHz frequencies and long wavelengths (tens of kilometers) relative to density stratification scale heights (fig. S4). Lamb waves (*6*) are AGWs propagating along Earth's surface, with group velocities near the mean sound speed of the lower atmosphere (~310 m/s for a 16 km scale height above Earth's surface (*7*)). Lamb waves are associated with the largest atmospheric explosions from volcanic eruptions (*8*) and nuclear tests (*9*) and have periods on the order of several to hundreds of minutes. Audible sound refers to higher frequency acoustic waves that can be heard by humans. Infrasound (*10*) refers to acoustic waves

below the standard audio range. The crossover between audible and infrasound is often given as 20 Hz.

Of the atmospheric waves produced by the climactic Hunga explosion, the most prominent is the Lamb wave ($f \lesssim 0.01$ Hz), which propagates efficiently and is detected globally by numerous ground-based and spaceborne geophysical instrumentation systems (Fig. 1A; fig. S5) (Movies S1–S6). Despite the Lamb wave′s large amplitude, its waveform pressure increase as a function of time (rise-time) is relatively slow and does not have characteristics of a shock wave. Over six days, we observed global propagation of at least four minor-arc Lamb wave passages (A1,3,5,7) and three (A2,4,6) major-arc (antipodal) passages (Fig. 1A inset; Fig. 2A,B; fig. S6A).

The number of Lamb wave passages observed for Hunga (4 + 3 antipodal) is approximately the same as observed for the 1883 Krakatau eruption (*11*, *12*) (Fig. 2A). The exceptional spatiotemporal resolution of the evolving wavefield from 2022 Hunga, in comparison to 1883 Krakatau, is a consequence of more than a century of advances in instrumentation technology and global sensor density (Fig. 1A). Measurements of Lamb wave peak-to-peak pressure amplitudes as a function of distance indicate that the atmospheric pressure pulse generated by the Hunga event is comparable to that of the 1883 Krakatau eruption (*12*) (Fig. 2F; fig. S8). However, the Krakatau Lamb pulse was approximately 30% longer-duration than that of Hunga at comparable stations (Fig. 2A). Peak-to-peak pressure amplitudes from Hunga generally decreased logarithmically from 1,473 Pa (756 km) with range (Fig. 2F; fig. S9). We infer that the notable scatter in amplitudes at distances >7,500 km is related to winds and wavefront focusing around the spherical Earth (*3*), as well as a potentially anisotropic source. The Hunga signal amplitudes are over an order of magnitude larger than those generated by the 1980 Mount St. Helens eruption (*13*).

Equivalent explosive yields for large volcanic eruptions have previously been estimated using pressure recordings, but quantitative comparisons with non-volcanic sources are problematic. During the 1950s–1960s atmospheric nuclear testing era, theoretical and empirical relationships were generated relating AGW amplitudes and periods to explosive yield (*14, 15*). We find that such relationships are inapplicable to the signals generated by Hunga, as they result in unphysically large equivalent yields (*3*) (fig. S10A). This difference is presumably because, for a given energy release, the long-duration climactic eruption excites longer-period pressure disturbances than the near-instantaneous nuclear reaction (fig. S10B). Hunga signals have peak-to-peak pressures comparable to those produced by the largest historical atmospheric nuclear test (58 Mt, USSR, 1961) (*16*), but the dominant eruption signal periods (1,700–2,500 s) are approximately four times longer than those of the anthropogenic explosion (400–700 s) (*17*).

The Hunga eruption pressure waves have complex waveform and spectral characteristics, likely related to both source and propagation. The Lamb wave is the largest-amplitude pressure wave arrival (Fig. 2B) (*3*). Near Hunga, the Lamb wave consists of at least two pulses and begins with a 7–10 min pressure increase, followed by a second larger compression and subsequent long rarefaction phase (Figs. 1A,2). This sequence is different from a single bipolar pulse typical of large anthropogenic explosions (*18*). The shallow-submarine volcanic source presumably contributes to this waveform complexity (*19*). The Lamb wave period ranges between 0.3–10 mHz (3,300–100 s) and the group velocity is ~315 m/s (*3, 20*) (fig. S11). Each subsequent antipodal passage produces an observed 90˚ phase shift in the Lamb wave (*21*) (fig. S12). This 90˚ phase

shift is expected by comparison of the asymptotic forms of the equation for a traveling wave on the surface of a sphere from before the antipodal crossing to that from after crossing (*21*, *22*). The Lamb wave is composed of several AGW modes, and the Hunga signals show distinct dispersion at higher frequencies (fig. S13), which was similarly noted for other large AGW signals (*20*). Some barometer observations also show the arrival of a lower velocity gravity wave (figs. S11,S14).

The climactic Hunga eruption also produced remarkable long-range infrasound (f ~0.01–20 Hz), clearly detected at most IMS infrasound arrays (fig. S15) as well as numerous regional arrays and networks (*3*) (Table S4; figs. S16–S21). Infrasound signals arrive after the Lamb wave; at most stations, the Lamb wave dominates below ~0.01 Hz, followed by broadband infrasound (Fig. 3). The IMS infrasound network recorded at least two direct and two antipodal infrasonic wave arrivals from the main explosive event. At most of the infrasound stations, array processing indicates direct infrasonic arrivals for ~2 hrs with group velocities between 250 to 290 m/s (*3*) (fig. S15). Infrasound amplitudes following the first Lamb wave arrival A1 are on the order of several pascals, and are observed to decrease with each global wave passage (Fig. 2F). Complex waveform interference effects are observed for stations near the source and the antipode, where the wavetrains of successive arrivals overlap (*3*). Prominent time evolution in signal back-azimuth and apparent velocity is observed at many infrasound arrays, especially at stations for which the propagation path crosses the circumpolar vortex (*3*) (fig. S22).

Accounts of audible sound (f > 20 Hz) were reported across Alaska as far as 10,000 km from Hunga (compared to ~4,800 km for Krakatau 1883; (*12*)) and are verified by ~30 min duration signals on higher-sample-rate low-frequency microphone stations (Fig. 3E). The audio signals arrive after the Lamb wave and at the end of the infrasound wavetrain, and consist of short-duration impulsive signals consistent with repeated "booms" reported by observers. Linear propagation and attenuation models cannot explain the high-frequency infrasound and audible sound at these extreme ranges, implying nonlinearity in generating the higher frequencies along the propagation path (*3*, *13*). Evidence of nonlinearity in Fig. 3E is two-fold. First, the high-frequency spectral slope during the "peak" time window approximates that of an ideal shock wave in its old-age (*3*) (but still nonlinear) decay: f^{-2}, followed by a faster exponential roll-off at frequencies where atmospheric absorption dominates nonlinearity. Second, the impulsive events, when separated from the lower-frequency, higher-amplitude infrasound portion by filtering (from 10 to 40 Hz), have coarsely sampled *N*-wave shapes reminiscent of explosions or sonic booms. Dramatic increases in global population and advances in societal connectivity (e.g., internet vs. telegraph) presumably contribute to the enhanced reports of audibility at distances greater than those historically documented for Krakatau and other large events.

Due to the extraordinary amplitude of the Lamb wave, it produced coupled signals at multi-technology stations (Fig. 2E); (*3*). For example, in the Mediterranean, the Lamb wave produced signals on hydrophones at ~50 m water depth near Stromboli volcano, 17,740 km from Hunga (*3*) (fig. S17B).

Seismometers worldwide recorded ground motions associated with both pure seismic waves (figs. S2,S23) and air-to-ground coupled atmospheric waves (Fig. 3; figs. S24,S6B). We associate the most prominent seismic (*P*, *S*, and Rayleigh waves) and atmospheric arrivals (Fig. 2) with the main eruption at 04:14:45 UTC, which had a reported M_w 5.7–5.8. Our observations of multiple overlapping seismic phases (Fig. 2D) suggest a longer-duration source process, with at least two

discrete events and multiple phases. Additionally, seismic ground motions globally exhibit a marked spectral peak at 3.7 mHz (Fig. 3D). We interpret this peak as Rayleigh-wave propagation (corresponding to Earth normal mode ${}_0S_{29}$) resulting from the coupling of fundamental acoustic mode oscillations of the atmosphere near the volcanic source into the solid Earth (*3*) (fig. S25). This solid Earth mode was also excited during the 1991 eruption of Mount Pinatubo (*23*); however, the seismic oscillations generated by the climactic 2022 Hunga eruption are over an order of magnitude larger (*3*).

Numerous additional Earth observation systems recorded the atmospheric waves from the climactic eruption. Data from neutral atmospheric radio occultations (ROs), satellite-based radiometers, and dual-frequency GNSS receivers, in conjunction with data from ground-based infrasound stations and a DART (Deep-ocean Assessment and Reporting of Tsunamis) buoy (1,225 km), reveal strong seismo- and hydro-atmospheric coupling in the aftermath of the eruption (Fig. 4). The Lamb wave arrival time at IS-II (station CTAO, 3,997 km) is consistent with that obtained using brightness temperature differences measured by the Himawari-8 satellite (*3*) (fig. S5). At this time, an RO profile over Eastern Australia (RO-III, 3,781 km) clearly displays heightened gravity-wave activity in the stratosphere. In the hours after the eruption, ROs in the vicinity of Hunga (RO-I, 366 km, and RO-II, 453 km) also reveal strong gravity wave activity in the stratosphere with temperature perturbations of ±4 K, four times the typical background activity.

The atmospheric waves also propagated to the ionosphere, where 1 Hz data recorded in real-time by ground-based GNSS stations can be converted to ionospheric total electron content (TEC). TEC data clearly demonstrate wave-like structures of unprecedented magnitude traveling between ~320 and 1,000 m/s. TEC profiles (G-I and G-II) collocated with infrasound stations IS-I (station MSVF, 756 km) and IS-II show the arrival of the Lamb wave in the ionosphere ~24 min after it is recorded at the infrasound station (propagating at an apparent vertical velocity of ~312 m/s for an assumed ionospheric shell height of 450 km). Similar to the global barometer data (Fig. 2B), the Lamb wave was observed worldwide in TEC data. In addition, a DART buoy (B-I) and a nearby TEC record (G-III) north of Hunga record tsunami-like waves generated by the atmospheric pulse (i.e., air-sea waves; (*8*)), one hour before the appearance of tsunami signatures of direct volcanic origin (*3*) (fig. S26).

Understanding these geophysical observations from the Hunga eruption requires accurate propagation modeling. However, simulating atmospheric wave propagation is challenging here for multiple reasons. (i) The complexity of the highly-energetic, shallow submarine, and multiphase eruption is beyond existing capability for modeling the source and the subsequent repartition of energy among the different waves (*3*). (ii) The physical problem involves multiple scales. Indeed, observed atmospheric waves contain energy extending from the acoustic-gravity regime, including a strong Lamb wave, through the infrasonic range, and into audio frequencies (Fig. 3). (iii) Atmospheric wave propagation is strongly nonlinear, which leads to energy cascading into higher frequencies even far from the event. For such energetic events, wave propagation nonlinearities remain important far from the source. Considering (ii) and (iii) together, the challenge is due to the nonlinear energy cascading that couples these various regimes (acoustic-gravity, infrasound, audio) and requires modeling methods that account for that coupling. (iv) Finally, substantial temporal and spatial variations of atmospheric conditions along propagation paths render a stratified atmospheric model inappropriate. Existing propagation algorithms (based, for instance, on the equations of fluid mechanics, the parabolic approximation of the wave equation, normal-mode summation, or ray tracing; (*3*)) are limited in their physics and computational feasibility (fig.

S27). Nevertheless, preliminary simulations (*3*) find notable departures of predicted propagation paths from great circle paths (fig. S28; Movie S7), which leads to direction-of-arrival deviations qualitatively in agreement with observations (fig. S22; Table S5).

The impacts of volcanic atmospheric waves are usually limited, but sometimes shock waves from strong volcanic explosions damage nearby infrastructure (*24*, *25*). Atmospheric waves from the main Hunga eruption had far more extensive impacts. Unusual sea level changes or tsunamis were observed in the Pacific earlier than predicted, and in the Caribbean and Mediterranean without direct ocean routes. We report observations of early sea level oscillations in the Pacific (*3*). At coastal tide gauges, the tsunami onset time coincides approximately with the Lamb wave arrival (2 hPa pulse); the tsunami onset is unclear, but wave amplitudes gradually increase over 2–4 hrs to >1 m in some locations. In contrast, deep-sea tsunamimeters record a clear leading 5 hPa pressure pulse, more than double that of the air-pressure pulse (*3*) (figs. S29,30). Air-sea coupling (*8*, *26*) likely caused these exceptional observations, and should be considered in future scenarios for tsunami early-warning systems.

Geophysical records of the January 2022 Hunga eruption represent an unparalleled global dataset of atmospheric wave generation and propagation, providing an opportunity for multi-technology observation, modeling, and validation unprecedented in the modern record. The datasets highlighted here are not exhaustive; there is outstanding potential for augmenting details of the global wavefield capture through incorporating numerous additional interdisciplinary datasets, including citizen-science data (*27, 28*). The January 2022 Hunga eruption presents an extraordinary opportunity to advance understanding of rarely captured physical phenomena, including global Lamb wave propagation, atmospheric free-oscillations coupling with the solid Earth, nonlinear energy cascading in atmospheric wave propagation, excitation of infrasound and audible sound at global distances, air-sea waves, and many others.

References and Notes

1. The name of the volcano is “Hunga”, not “Hunga Tonga”. “Hunga” relates to the entire volcano, rather than the islands. “Hunga Tonga” refers specifically to the southwestern island of the two.
2. R. G. Vaughan, P. W. Webley, Satellite observations of a surtseyan eruption: Hunga Ha’apai, Tonga. *J. Volcanol. Geotherm. Res.* **198**(1-2) 177-186 (2010).
3. Materials and methods and data and network citations are available as supplementary materials.
4. E. E. Gossard, W. H. Hooke, Waves in the atmosphere: atmospheric infrasound and gravity waves - their generation and propagation. (*Elsevier*, Amsterdam, 1975).
5. K. C. Yeh and C. H. Liu, Acoustic-gravity waves in the upper atmosphere. *Rev. Geophys.* **12**(2) 193-216 (1974).
6. H. Lamb, On atmospheric oscillations. *Proc. R. Soc. Lond. A*, 84551–572 (1911).
7. F. P. Bretherton, Lamb waves in a nearly isothermal atmosphere, *Quart. J. R. Met. Soc.*, 95, 754-757 (1969). doi:10.1002/qj.49709540608

8. D. Harkrider, F. Press, The Krakatoa air-sea waves: An example of pulse propagation in coupled systems. *Geophys. J.R. astr. Soc.* **13**(1-3), 149-159 (1967).

9. A. D. Pierce, J. W. Posey, Theory and propagation of Lamb's atmospheric edge mode from nuclear explosions. *Geophys. J. Int.* **26**(1-4), 341-368 (1971).

10. R. Matoza, D. Fee, D. Green, P. Mialle, Volcano infrasound and the International Monitoring System, in Infrasound monitoring for atmospheric studies: Challenges in middle-atmosphere dynamics and societal benefits, A. Le Pichon, E. Blanc, and A. Hauchecorne, Eds. 1023-1077, (*Springer, Cham*, 2019). doi:10.1007/978-3-319-75140-5_33

11. R. H. Scott, I. Note on a series of barometrical disturbances which passed over Europe between the 27th and the 31st of August, 1883. *Proc. R. Soc. Lond.* **36**, 139-143 (1883).

12. R. H. Strachey, On the air waves and sounds caused by the eruption of Krakatoa in August 1883. in The eruption of Krakatoa and subsequent phenomena, Report of the Krakatoa Committee of the Royal Society G. J. Symons, Ed. (*Trübner and Co*, 1888).

13. J. W. Reed, Air pressure wave from Mount St. Helens eruptions. *J. Geophys. Res. Atmos.* **92**(D10), 11979-11992 (1987).

14. J. W. Posey, A. D. Pierce. Estimation of nuclear explosion energies from microbarograph records. *Nature* **232**(5308) 253–253 (1971).

15. G. B. Olmsted, Detection of airborne low-frequency sound from nuclear explosions. *United States Air Force, Office for Atomic Energy, Operation Castle Report* WT-931 (1955)

16. W. L. Donn, D. M. Shaw, A. C. Hubbard, The microbarographic detection of nuclear explosions. *IEEE Trans. Nucl. Sci.* **10**(1) 285-296 (1963)

17. A. D. Pierce, C. A. Moo, J. W. Posey, Generation and propagation of infrasonic waves. *Air Force Cambridge Research Laboratories*, AFCRL-TR-73-0135 (1973).

18. D. Fee, R. Waxler, J.D. Assink, Y. Gitterman, J. Given, J. Coyne, P. Mialle, M. Garces, D. Drob, D. Kleinert, R. Hofstetter, P. Grenard, Overview of the 2009 and 2011 Sayarim infrasound calibration experiments. *J. Geophys. Res. Atmos.* **118**(12) 6122-6143 (2013).

19. J. J. Lyons, M. M. Haney, D. Fee, W. G. Wech, C. F. Waythomas, Infrasound from giant bubbles during explosive submarine eruptions. *Nat. Geosci.*, **12** 952–958 (2019). https://doi.org/10.1038/ s41561-019-0461-0

20. F. Press, D. Harkrider, Propagation of acoustic-gravity waves in the atmosphere. *J. Geophys. Res.* **67**(10) 3889-908 (1962).

21. J. N. Brune, J. E. Nafe, L. E. Alsop, The polar phase shift of surface waves on a sphere. *Bull. Seismol. Soc. Am.* **51**(2) 247–257 (1961). doi: https://doi.org/10.1785/BSSA0510020247.

22. J. H. Ansell, Legendre functions, the Hilbert transform and surface waves on a sphere. *Geophys. J. Int.*, 32, 1, 95-117 (1973). doi:10.1111/j.1365-246X.1973.tb06522.x

23. S. Watada, H. Kanamori, Acoustic resonant oscillations between the atmosphere and the solid earth during the 1991 Mt. Pinatubo eruption, *J. Geophys. Res.* **115**, B12319, (2010). doi:10.1029/2010JB007747

24. K. Kato, H. Yamasato, The 2011 eruptive activity of Shinmoedake volcano, Kirishimayama, Kyushu, Japan - Overview of activity and Volcanic Alert Level of the Japan Meteorological Agency. *Earth Planet Sp.* **65** 2 (2013). doi:10.5047/eps.2013.05.009

25. G. A. Valentine, Damage to structures by pyroclastic flows and surges, inferred from nuclear weapons effects. *J. Volcanol. Geotherm. Res.* **87**(1-4), 117-140 (1998).

26. J. Proudman, The effects on the sea of changes in atmospheric pressure. *Geophysical Supplements to the Monthly Notices of the Royal Astronomical Society*, 2(4), 197-209 (1929) doi:10.1111/j.1365-246X.1929.tb05408.x

27. A. M. Portas, L. Barnard, C. Scott, G. R. Harrison, The National Eclipse Weather Experiment: use and evaluation of a citizen science tool for schools outreach. *Phil. Trans. R. Soc.*, A.3742015022320150223 (2016) doi:10.1098/rsta.2015.0223

28. E. Calais, S. Symithe, T. Monfret, B. Delouis, A. Lomax, F. Courboulex, J. P. Ampuero, P. E. Lara, Q. Bletery, J. Chese, F. Peix, A. Deschamps, B. De Lepinay, B. Raimbault, R. Jolivet, S. Paul, S. St Fleur, D. Boisson, Y. Fukushima, Z. Duputel, L. Xu, L. Meng, Citizen seismology helps decipher the 2021 Haiti earthquake, *Science* (2022): eabn1045, doi:10.1126/science.abn1045

References and Notes for Supplementary Material

29. M. Beyreuther, R. Barsch, L. Krischer, T. Megies, Y. Behr, J. Wassermann, ObsPy: A Python toolbox for seismology. *Seismol. Res. Lett.* **81**, 530-533 (2010).

30. T. K. Ahern, B. Dost, SEED standard for the exchange of earthquake data reference manual format version 2.4. Incorporated Research Institutions for Seismology (IRIS) (2012).

31. A. Rohatgi, WebPlotDigitizer. https://automeris.io/WebPlotDigitizer (2020).

32. R. G. Harrison, Pressure anomalies from the January 2022 Hunga Tonga-Hunga Ha'apai eruption. Weather 77, 87–90 (2022). doi:10.1002/wea.4170

33. R. G. Harrison, Tonga eruption atmospheric pressure wave data. *University of Reading. Dataset.* (2022) https://doi.org/10.17864/1947.000354

34. S. N. Gurbatov, O. V. Rudenko, Statistical phenomena in *Nonlinear Acoustics*, M. F. Hamilton, D. T. Blackstock, Eds. (Academic, San Diego, 1998), pp. 377-398.

35. R. L. Parker, PSD: Power Spectra by Sine Multitapers. Retrieved from: https://igppweb.ucsd.edu/~parker/Software/ (2014, March 9).

36. H. Kanamori, J. Mori, D. G. Harkrider, Excitation of atmospheric oscillations by volcanic eruptions. *J. Geophys. Res. Solid Earth* **99**, 21947–21961 (1994).

37. R. Ware, M. Exner, D. Feng, M. Gorbunov, K. Hardy, B. Herman, Y. Kuo, T., Meehan, W. Melbourne, C. Rocken, W. Schreiner, S. Sokolovskiy, F. Solheim, X. Zou, R. Anthese, S. Businger, K. Trenberth, GPS sounding of the atmosphere from low earth orbit: Preliminary results. *Bull. Am. Meteorol. Soc.* **77**, 19–40 (1996).

38. R. A. Anthes, Exploring Earth's atmosphere with radio occultation: contributions to weather, climate and space weather. *Atmos. Meas. Tech.* **4**, 1077–1103 (2011).

39. W. S. Schreiner, J. P. Weiss, R. A. Anthes, J. Braun, V. Chu, J. Fong, D. Hunt, Y. H. Kuo, T. Meehan, W. Serafino, J. Sjoberg, S. Sokolovskiy, E. Talaat, T. K. Wee, Z. Zeng, COSMIC-2 Radio Occultation Constellation: First Results. *Geophys. Res. Lett.* **47(4)**, e2019GL086841 (2020).

40. N. E. Bowler, An assessment of GNSS radio occultation data produced by Spire. *Q. J. R. Meteorol. Soc.* **146**, 3772–3788 (2020).

41. G. Blewitt, An Automatic Editing Algorithm for GPS data. *Geophys. Res. Lett.* **17**, 199–202 (1990).

42. P. J. G. Teunissen, O. Montenbruck, *Springer Handbook of Global Navigation Satellite Systems*. (Springer, Cham, 2017).
43. G. Mungov, M. Eblé, R. Bouchard, DART® Tsunameter Retrospective and Real-Time Data: A Reflection on 10 Years of Processing in Support of Tsunami Research and Operations. *Pure Appl. Geophys.* **170**, 1369–1384 (2013).
44. J. Marty, "The IMS Infrasound Network: Current Status and Technological Developments" in *Infrasound monitoring for atmospheric studies: Challenges in middle-atmosphere dynamics and societal benefits*, A. Le Pichon, E. Blanc, and A. Hauchecorne, Eds. 3-62 (Springer, Cham, 2019). https://doi.org/10.1007/978-3-319-75140-5_15
45. P. Mialle, D. Brown, N. Arora, colleagues from IDC "Advances in Operational Processing at the International Data Centre", in *Infrasound monitoring for atmospheric studies: Challenges in middle-atmosphere dynamics and societal benefits*, A. Le Pichon, E. Blanc, and A. Hauchecorne, Eds. 209-248 (Springer, Cham, 2019). https://doi.org/10.1007/978-3-319-75140-5_6
46. L.G. Evers, "The inaudible symphony: On the detection and source identification of atmospheric infrasound", thesis, TU Delft (2008).
47. Y. Cansi, An automatic seismic event processing for detection and location: The PMCC method. *Geophys. Res. Lett.* **22**, 1021-1024 (1995).
48. K. Nishida, N. Kobayashi, Y. Fukao, Background Lamb waves in the Earth's atmosphere. *Geophys. J. Int.* **196**(1), 312–316 (2014).
49. T. Gabrielson, Krakatoa and the Royal Society: the Krakatoa explosion of 1883. *Acoust Today*. **6**(2), 14-19 (2010).
50. F. Press, D. Harkrider, Air-sea waves from the explosion of Krakatoa. *Science*, **154**(3754), 1325-1327 (1966).
51. W. L. Donn, N. K. Balachandran, Mount St. Helens eruption of 18 May 1980: Air waves and explosive yield. *Science* **213**(4507), 539-541 (1981).
52. M. Tahira, M. Nomura, Y. Sawada, K. Kamo, "Infrasonic and acoustic-gravity waves generated by the Mount Pinatubo eruption of June 15, 1991" in *Fire and Mud: Eruptions and Lahars of Mount Pinatubo, Philippines*. 601-614 (1996).
53. C. E. Needham, *Blast waves* (Springer, New York, 2010).
54. D. Fee, R. S. Matoza, An overview of volcano infrasound: From Hawaiian to Plinian, local to global. *J. Volcanol. Geotherm. Res.* **249**, 123-139 (2013).
55. G. F. Kinney, K. J. Graham, *Explosive shocks in air* (Springer Science & Business Media, 2013).
56. D. O. Revelle, Historical detection of atmospheric impacts by large bolides using acoustic-gravity waves. *Los Alamos National Laboratory, NM (United States)* Technical Report LA-UR-95-1263 (1995).
57. M. Ripepe, D. Delle Donne, R. Genco, G. Maggio, M. Pistolesi, E. Marchetti, G. Lacanna, G. Ulivieri, P. Poggi, Volcano seismicity and ground deformation unveil the gravity-driven magma discharge dynamics of a volcanic eruption. *Nat Commun.* **6**, 6998 (2015).
58. J. Capon, Investigation of long-period noise at the large aperture seismic array. *J. Geophys. Res.* **74**(12), 3182-3194 (1969).
59. G. G. Sorrells, J. A. McDonald, Z. A. Der, E. Herrin, Earth Motion Caused by Local Atmospheric Pressure Changes. *Geophy. J. Int.* **26**(1-4), 83–98 (1971).
60. P. W. Rodgers, The response of the horizontal pendulum seismometer to Rayleigh and Love waves, tilt, and free oscillations of the Earth. *Bull. Seismol. Soc. Am.* **58**(5), 1385-1406 (1968).
61. R. Raspet, C. J. Hickey, B. Koirala, Corrected Tilt Calculation for Atmospheric Pressure-Induced Seismic Noise. *Appl. Sci.* **12**(3), 1247 (2022).

62. L. M. Rolland, G. Occhipinti, P. Lognonné, A. Loevenbruck, Ionospheric gravity waves detected offshore Hawaii after tsunamis. *Geophys. Res. Lett.* **37**, L17101 (2010).
63. R. Waxler, J. D. Assink, "Propagation Modeling Through Realistic Atmosphere and Benchmarking" in *Infrasound monitoring for atmospheric studies: Challenges in middle-atmosphere dynamics and societal benefits*, A. Le Pichon, E. Blanc, and A. Hauchecorne, Eds. 509–549 (Springer, Cham, 2019). https://doi.org/10.1007/978-3-319-75140-5_15
64. P. Blom, Modeling infrasonic propagation through a spherical atmospheric layer – Analysis of the stratospheric pair. *J. Acoust. Soc. Am.* **145**(4), 2198-2208 (2019).
65. R. Waxler, C. Hetzer, J. D. Assink., D. Velea, chetzer-ncpa/ncpaprop-release: NCPAprop Version 2.1.0, Zenodo (2021). https://doi.org/10.5281/zenodo.5562713
66. H. Hersbach, B. Bell, P. Berrisford, G. Biavati, A. Horányi, J. Muñoz Sabater, J. Nicolas, C. Peubey, R. Radu, I. Rozum, D. Schepers, A. Simmons, C. Soci, D. Dee, J.-N. Thépaut, (2018) *ERA5 hourly data on pressure levels from 1979 to present.* Copernicus Climate Change Service (C3S) Climate Data Store (CDS). (Accessed on 15-02-2022), 10.24381/cds.bd0915c6
67. D. P. Drob, J. M. Picone, M. Garcés, Global morphology of infrasound propagation. *J. Geophys. Res. Atmos.* **108**(D21), 4680 (2003).
68. J. M. Picone, A. E. Hedin, D. P. Drob, A. C. Aikin, NRLMSISE-00 empirical model of the atmosphere: Statistical comparisons and scientific issues. *J. Geophys. Res. Space Phys.* **107**(A12), SIA-15 (2002).
69. D. P. Drob, J. T. Emmert, J. W. Meriwether, J. J. Makela, E. Doornbos, M. Conde, G. Hernandez, J. Noto, K. A. Zawdie, S. E. McDonald, J. D. Huba, J. H. Klenzing, An update to the Horizontal Wind Model (HWM): The quiet time thermosphere. *Earth Space Sci.* **2**(7) 301-319 (2015).
70. P. S. M. Smets, J. D. Assink, A. Le Pichon, L. G. Evers, ECMWF SSW forecast evaluation using infrasound. *J. Geophys. Res. Atmos.* **121**(9), 4637-4650 (2016).
71. J. D. Assink, R. Waxler, P. Smets, L. G. Evers, Bidirectional infrasonic ducts associated with sudden stratospheric warming events. *J. Geophys. Res. Atmos.* **119**(3), 1140-1153 (2014).
72. W. L. Donn, The Microbarovariograph: A New Instrument For Measuring Minute Atmospheric Pressure Variations. *Trans. Am. Geophys. Union*, **39**(2), 366-368(1958). https://doi.org/10.1029/TR039i002p00353
73. D. G. Harkrider, Theoretical and observed acoustic-gravity waves from explosive sources in the atmosphere. *J. Geophys. Res.* **69**(24), 5295-5321 (1964).
74. S. Shani-Kadmiel, G. Averbuch, P. Smets, J. Assink, L. Evers, The 2010 Haiti earthquake revisited: An acoustic intensity map from remote atmospheric infrasound observations. *Earth Planet Sci. Lett*. **560**, 116795 (2021).
75. A. Levshin, L. Ratnikova, J. Berger, Peculiarities of Surface-Wave Propagation across Central Eurasia." *Bull. Seismol. Soc. Am.* **82**(6), 2464–2493 (1992).
76. M. M. Haney, D. Fee, K. F. McKee, J. J. Lyons, R. S. Matoza, A. G. Wech, G. Tepp, C. Searcy, T. D. Mikesell, Co-eruptive tremor from Bogoslof volcano: seismic wavefield composition at regional distances. *Bull. Volcanol.* **82**, 18 (2020).
77. A. M. Dziewonski, D. L. Anderson, Preliminary reference Earth model, *Phys. Earth Planet. Inter.* **25**(4), 297-356 (1981).
78. P. Lognonné, E. Clévédé, H. Kanamori, Computation of seismograms and atmospheric oscillations by normal-model summation for a spherical earth model with realistic atmosphere. *Geophy. J. Int.* **135**(2), 388-406 (1998).
79. C. Amante, B. W. Eakins, *ETOPO1: 1 Arc-Minute Global Relief Model: Procedures, Data Sources and Analysis (NOAA Technical Memorandum NESDIS NGDC-24)*. (2009). DOI:10.7289/V5C8276M.

80. International Seismological Centre (2022), On-line Bulletin, https://doi.org/10.31905/D808B830
81. C. Pilger, P. Gaebler, P. Hupe, A. C. Kalia, F. M. Schneider, A. Steinberg, H. Sudhaus, L. Ceranna, Yield estimation of the 2020 Beirut explosion using open access waveform and remote sensing data. *Sci. Rep.* **11**(1), 1-14 (2021).
82. G. S. Gorshkov, Gigantic eruption of the Volcano Bezymianny. *Bulletin Volcanologique* **20**, 77-109 (1959).
83. P. G. Brown, J. D. Assink, L. Astiz, R. Blaauw, M. B. Boslough, J. Borovicka, N. Brachet, D. Brown, M. Campbell-Brown, L. Cerenna, W. Cooke, C. de Groot-hedlin, D. P. Drob, W. Edwards, L. G. Evers, M. Garces, J. Gill, M. Hedlin, A. Kingery, G. Laske, A. Le Pichon, P. Mialle, D. E. Moser, A. Saffer, E. Silber, P. Smets, R. E. Spalding, P. Spurny, E. Tagliaferri, D. Uren, R. J. Weryk, R. Whitaker, Z. Krzeminski, A 500-kiloton airburst over Chelyabinsk and an enhanced hazard from small impactors. *Nature* **503**, 238-241 (2013).
84. M. Saderra Masó, The eruption of Taal volcano, January 30, 1911. *Dept. of the Interior, Weather Bureau, Manila Bureau of Printing* (1911).
85. V. H. Goerke, J. M. Young, R. K. Cook, Infrasonic observations of the May 16, 1963, volcanic explosion on the Island of Bali. *J. Geophys. Res.* **70**(24), 6017-6022 (1965).
86. B. A. Bolt, T. Tanimoto, Atmospheric oscillations after the May 18, 1980 eruption of Mount St. Helens. *Eos*, **62**(23), 529-530 (1981).
87. A. L. Dabrowa, D. N. Green, A. C. Rust, J. C. Phillips, A global study of volcanic infrasound characteristics and the potential for long-range monitoring. *Earth Planet Sci. Lett.* **310**(3-4), 369-379 (2011).
88. H. Wexler, W. A. Hass, Global atmospheric pressure effects of the October 30, 1961, explosion. *J. Geophys. Res.* **67**(10), 3875-3887 (1962).

Acknowledgments:

We thank Milton Garces, Aaron Wech, and two anonymous reviewers for their comments that improved the manuscript. LM, AK, and SK thank Angelyn Moore at JPL for her advice on processing GNSS data. The views expressed herein are those of the authors and do not necessarily reflect the views of the CTBTO Preparatory Commission. The views expressed in the article do not necessarily represent the views of the U.S. Department of Energy or the U.S. Government. This research was funded by the National Nuclear Security Administration, Defense Nuclear Nonproliferation Research and Development (NNSA DNN R&D). Any use of trade, firm, or product names is for descriptive purposes only and does not imply endorsement by the U.S. Government. This product article has been peer reviewed and approved for publication consistent with USGS Fundamental Science Practices (https://pubs.usgs.gov/circ/1367/). Distribution statement: Cleared for release.

Funding:

National Science Foundation grant EAR-1847736 (RSM, HDO, RNL)

Defense Threat Reduction Agency Nuclear Arms Control Technology program under contract HQ003421F0112 (DF, LT, AW, KMA)

US Geological Survey Alaska Volcano Observatory (DF, MMH, JL, HF)

US Geological Survey Hawaiian Volcano Observatory (ADJ)

National Science Foundation grant EAR-1901614 (DF)

National Science Foundation grant EAR-1952392 (AMI)

U.S. Department of Energy by the LLNL under Contract Number DE-AC52-07NA27344 (KK)

Jet Propulsion Laboratory, California Institute of Technology, under a contract with the National Aeronautics and Space Administration (SK, LM, PV, AK, MOM)

French Agence Nationale de la Recherche (ANR) under reference ANR-19-CE04-0003 and CNES for APR project UVTECGEOX (LR and EAM) and CNES APR project "RealDetect" (EA)

JSPS KAKENHI Grant Number 19K04034 (SW)

JSPS KAKENHI Grant Number 21K21353 (KN, SW, MI)

Royal Society Grant Number IES\R2\202007 (SDA)

Los Alamos National Laboratory award number 89233218CNA000001 (PB, JW)

Projects PAPIIT-UNAM-NI108219 and UCMEXUS-CONACYT (AAC)

Strategic Science Investment Funding to GNS Science, New Zealand within the Hazards and Risk Management Programme (GK)

Internal funding from Penn State College of Engineering (TG)

NASA Earth Surface and Interior Program under Ben Phillips, under a grant to R. Kahn at the NASA Goddard Space Flight Center (KFM)

UCMEXUS-CONACYT grant 699758 (GMP)

Proyecto Generación de capacidades para la difusión de alertas tempranas y para el desarrollo de instrumentos de decisión ante las amenazas sísmicas y volcánicas dirigidos al Sistema Nacional de Gestión de Riesgos (MCR, CR)

Basic Research Project of KIGAM GP2020-017 and GP2021-006 (IC, IP)

SAGE II – IDA Network Operations, #SU-19-1001-08-UCSD and IGPP/SIO/UCSD internal funding (CWE, RJM)

DARPA Cooperative Agreement HR00112120003 (JBS, RS)

This research was partly supported by the Earth Observatory of Singapore (EOS) via its funding from the National Research Foundation of Singapore and the Singapore Ministry of Education under the Research Centres of Excellence initiative. This work comprises EOS contribution number 432. (BT, DT, AP)

Author contributions:

RSM designed and led the research. AMI coordinated the Supplemental Materials. RSM, DF, JA, AMI, DG, KK, LT, TL, SK, JML, KN, KG, MH, HDO, QB, LM, LR, PV, AN, JP, SSK, AW, SA, CC, SW, AP, BT, PM, ALP, JV (Vergoz), PH, PB, RW, SDA, JBS, ATR, REA, AJ, GK, GA, MR, MI, EAM drafted the manuscript and processed and visualized the data as displayed in the main manuscript; LT, PB, and JML provided the Supplementary movies. All 76 authors took part in discussions and data analysis, contributed to the manuscript, contributed to the Supplemental Materials, performed a full interactive review of the original manuscript, and approved the

submitted version. Authors Matoza (RSM) through Ichihara (MI) are listed in approximate order of contribution; all other authors (Arciniega-Ceballos through Wilson) are listed alphabetically.

Competing interests: The authors declare that they have no competing interests.

Data and materials availability: A complete list of the data and materials availability and data acknowledgements can be found in the Supplemental Material document "Methods and Materials" Section 15.

Supplementary Materials

Materials and Methods

Supplementary Text

figs. S1 to S30

Tables S1 to S5

References (*29–89*)

Movies S1 to S7

Data S1 to S6

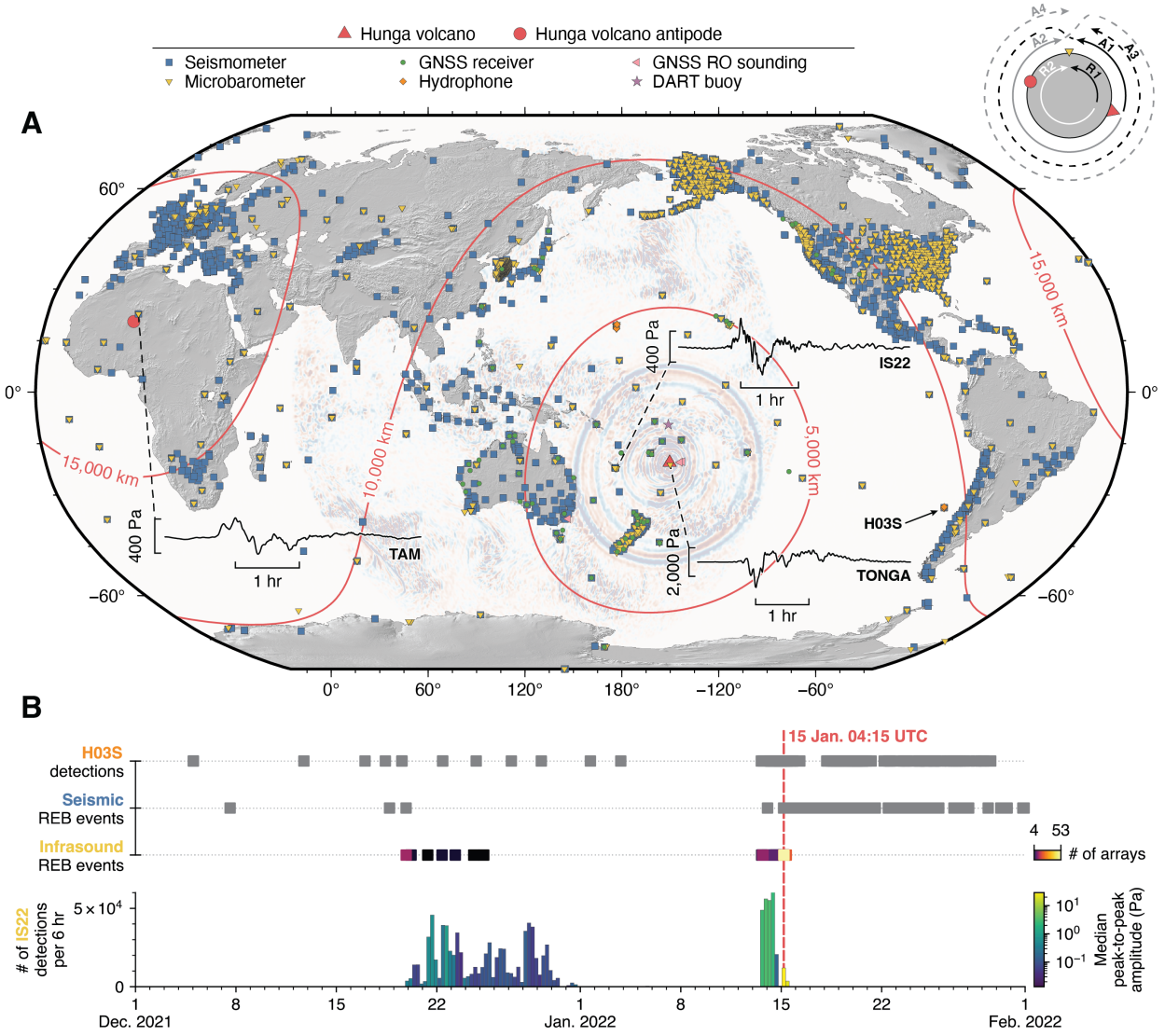

Fig. 1. Global distribution of recording geophysical sensors used in this study and remotely-observed eruption chronology. (**A**) Sensor map. Background image is brightness temperature difference (Himawari-8) at 07:10 UTC on 15 January 2022. Selected four-hour pressure waveforms are filtered 10,000–100 s. GNSS, Global Navigation Satellite System; RO, radio occultation; DART, Deep-ocean Assessment and Reporting of Tsunamis. Upper-right inset shows Hunga wave paths around Earth. (**B**) Hunga activity, December 2021 through January 2022, observed at IMS hydrophone, seismic, and infrasound stations (REB, Reviewed Event Bulletin); Hunga detections from nearest IMS infrasound array IS22 (1,848 km). Frequency responses for atmospheric pressure sensors used in this study are displayed in fig. S1.

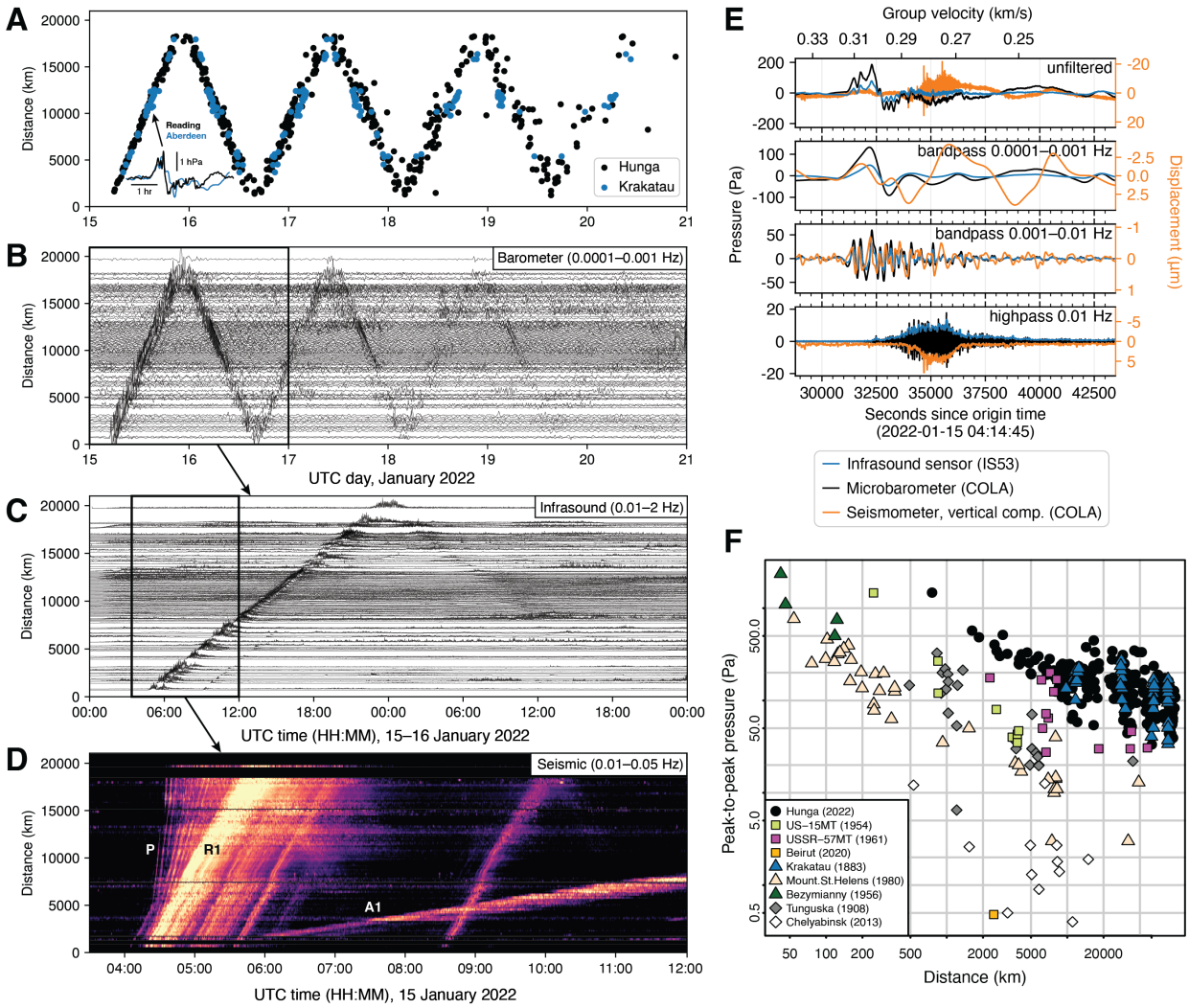

Fig. 2. Ground-based observations. (**A**) Lamb wave arrival times for 2022 Hunga (black) compared to 1883 Krakatau (blue); inset: Lamb A1 arrival waveform comparison (*3*). Global record sections of (**B**) barometer, (**C**) infrasound, and (**D**) seismic data showing the multiple arrivals and wave passages (see Fig. 1A inset); waveforms aggregated by radial distance (Fig. S7). A separate Rayleigh R1 is associated with the later ~08:31 event. (**E**) Colocated microbarometer (black), infrasound sensor (blue), and seismometer (orange) waveforms; lower panel shows inverted displacement envelope. (**F**) Wideband peak-to-peak pressure versus distance comparing 2022 Hunga with large historical explosive events (Table S2).

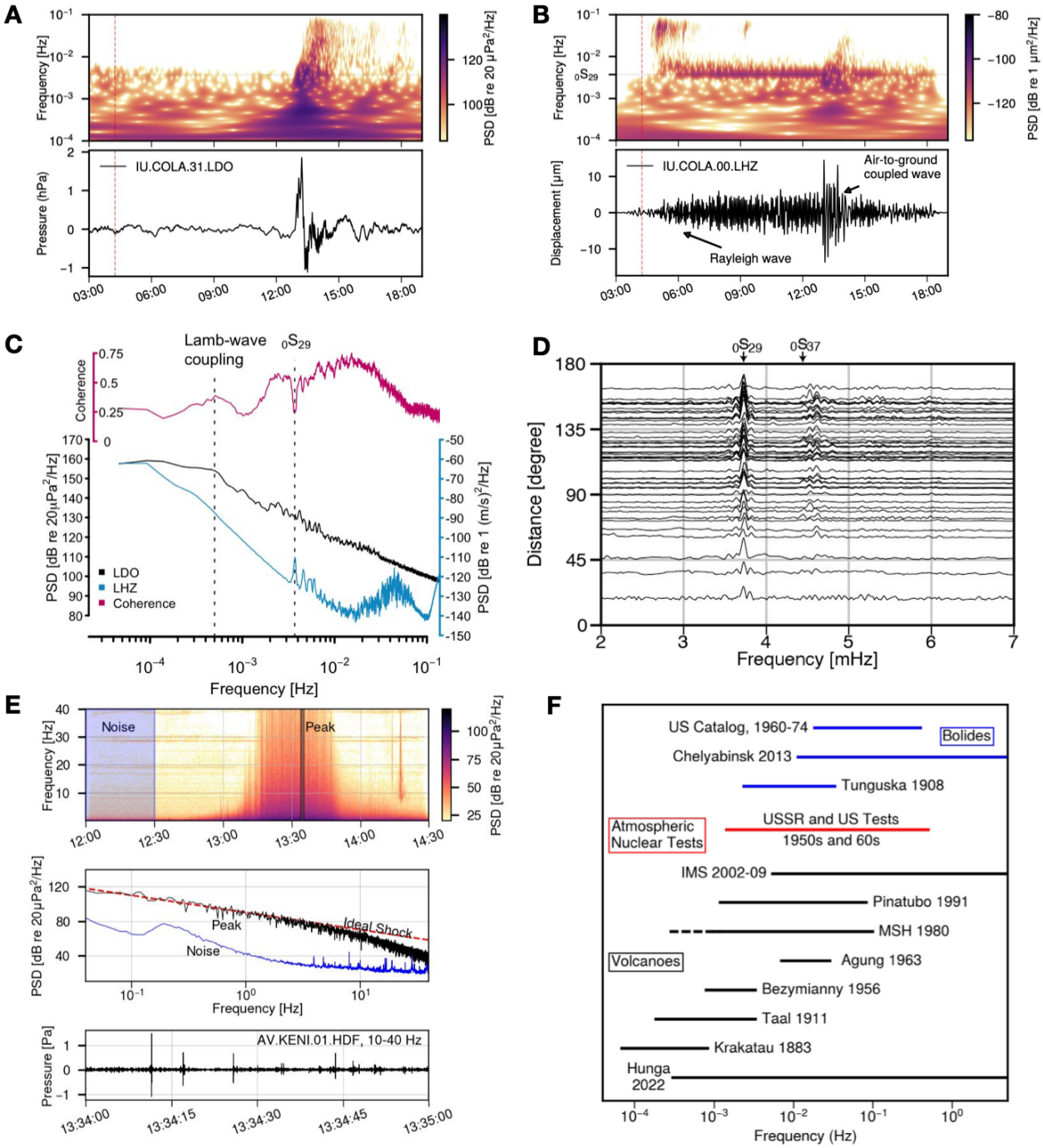

Fig. 3. Seismoacoustic spectral properties. Colocated wideband **(A)** pressure and **(B)** seismic spectrograms (top) and unfiltered waveforms (bottom). **(C, D)** Power spectral densities and seismoacoustic coherences worldwide show that pressure waves couple to the solid Earth through both (i) direct conversion as the Lamb wave passes the station and (ii) near-source excitation of atmospheric acoustic modes. (**E**) Alaska infrasound stations recorded audio range signals at great distances, apparent in the spectra (top) and as intermittent transients with shock-like features (middle and bottom panels). (**F**) Observed wideband pressure spectral character of Hunga compared to published instrumental observations of previous events (Table S3).

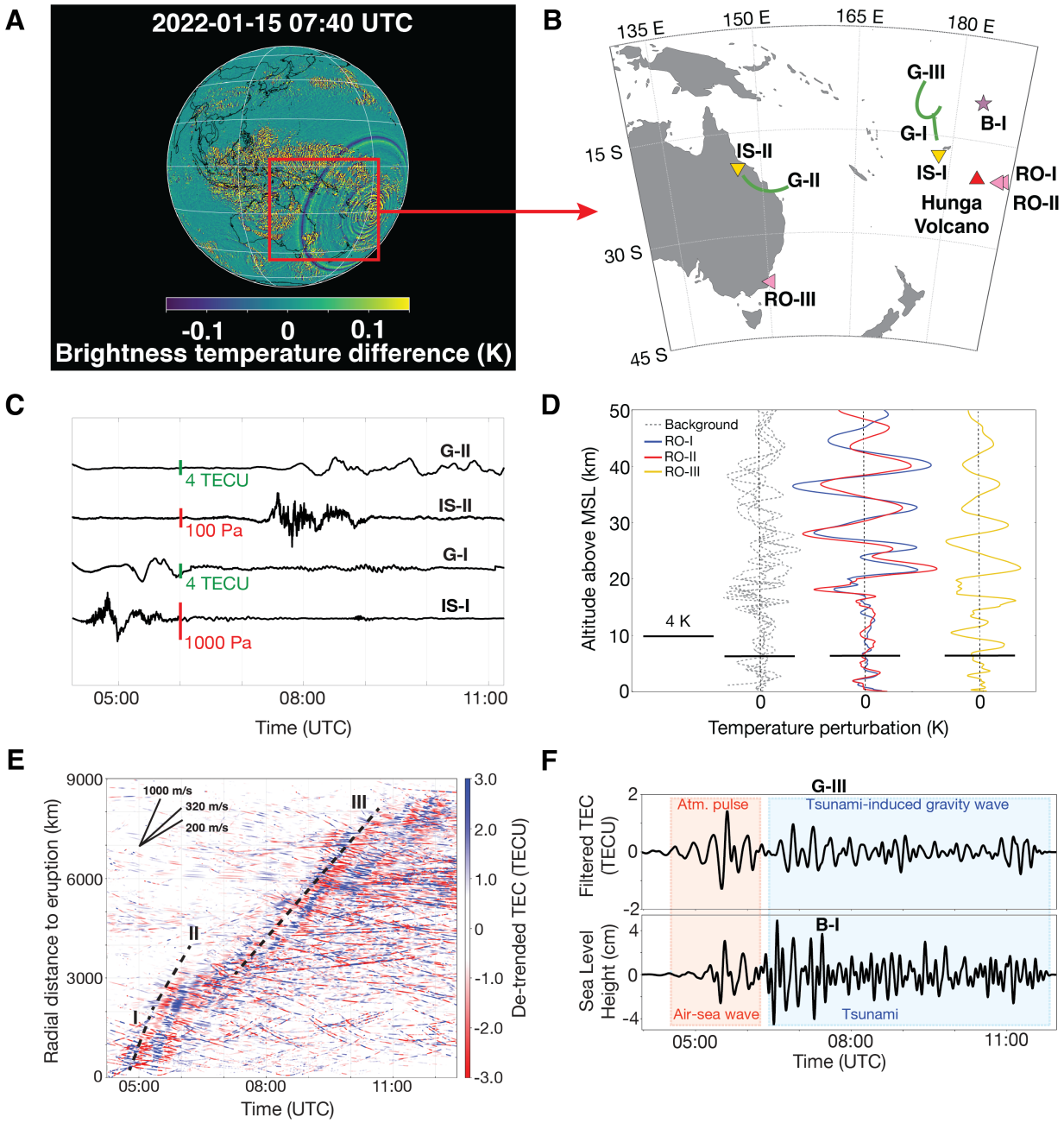

Fig. 4. Seismo- and hydro-atmospheric coupling from Earth's surface to space. (**A**) Brightness temperature variations in Himawari-8 data showing waves emanating from the Hunga eruption site. (**B**) Map of the inset in (A) with measurement locations in this figure. Ionospheric pierce point arcs (see Supplementary Material Section 14) are shown in green for the Lamb wave arrival for links G-I and G-II, and from 04:00 to 12:00 UTC for link G-III. (**C**) Infrasound (stations IS-I, IS-II) and TEC (GNSS links G-I and G-II) waveforms showing Lamb wave arrival; all signals high-pass filtered with 0.278 mHz (corresponding to 1-hr period) cutoff. (**D**) RO-I and RO-II at 06:50 UTC and 10:00 UTC showing strong coherent gravity wave activity several hours after the eruption; RO-III at 07:42 UTC also exhibits large gravity waves coincident with Himawari-8 data (A). (**E**) Hodochron plot of TEC records showing long-distance ionospheric wave propagation following the eruption. Features I and II are the first arrivals with different apparent wave velocities (551–1,333 m/s) due to the near-field wavefront curvature. Feature III, identified over 6,000 km

from the eruption, propagates at 478 m/s and is more likely linked to long-period gravity waves. (**F**) Buoy B-I data compared to TEC data from an adjacent GNSS link (G-III) showing efficient air-sea-air coupling across a broad frequency spectrum (*3*).